

Supporting Information

Highly intense NIR emissive Cu₄Pt₂ bimetallic clusters featuring Pt(I)-Cu₄-Pt(I) sandwich kernel

Rui-Ru Zhong,⁺ Mo Xie,⁺ Cui-Zhou Luan, Lin-Mei Zhang, De-Bo Hao, Shang-Fu Yuan,^{} and Tao Wu^{*}*

College of Chemistry and Materials Science, and Guangdong Provincial Key Laboratory of Functional Supramolecular Coordination Materials and Applications, Jinan University, Guangzhou 510632, P. R. China.

E-mail: sfyuan@jnu.edu.cn; wutao@jnu.edu.cn.

⁺These authors contributed equally to this work.

I. Experimental Section

Chemicals and Materials

Tetrakis(acetonitrile)copper(I) hexafluorophosphate ($\text{Cu}(\text{CH}_3\text{CN})_4\text{PF}_6$, 98%), potassium tetrachloroplatinate(II) (K_2PtCl_4 , 98%), 4-(trifluoromethyl) phenylacetylene ($\text{CF}_3\text{-PhC}\equiv\text{CH}$, 97%), 4-biphenylacetylene ($\text{BiPh-C}\equiv\text{CH}$, 97%), 2-ethynyl-naphthalene ($\text{Nap-C}\equiv\text{CH}$, 98%), 4-fluorophenylacetylene ($\text{F-PhC}\equiv\text{CH}$, 98%) were purchased from Bidepharm. Platinum(II) acetylacetone ($\text{Pt}(\text{acac})_2$, 97%) was purchased from Meryer; diphenyl-2-pyridylphosphine (dppy, 97%), 4-methoxyphenylacetylene ($\text{MeO-PhC}\equiv\text{CH}$, 98%) were purchased from Macklin; sodium hydroborate (NaBH_4 , AR) and other reagents employed were purchased from GHTECH. All reagents were used as received. $[\text{Cu}_8\text{H}_6(\text{dppy})_6](\text{PF}_6)_2$ was prepared according to the reported method.¹

II. Physical measurements

¹H and ³¹P NMR spectra were recorded on a Bruker Biospin Avance instrument (400 MHz). Fourier transform infrared (FT-IR) spectra were collected on Thermo Scientific FT-IR Nicolet iS10 spectrophotometer. Powder X-ray diffraction (PXRD) patterns were recorded on Rigaku Ultima IV X-ray Diffractometer ($\text{Cu K}\alpha$, $\lambda = 1.5418 \text{ \AA}$) in a step of 0.02° at 40 kV and 40 mA. X-ray photoelectron (XPS) spectroscopy spectra were performed by a Thermo ESCALAB 250XI system. Electron Paramagnetic Resonance (EPR) analysis was carried out on Bruker Magnetech ESR5000 in ESI, Bruker A300 in article. The solid-state UV-Vis-NIR diffuse reflection spectra and solution-state UV-vis spectra were recorded by with Agilent Cary 4000 UV-vis spectrophotometer. The PL and PLE spectra at room temperature were performed on an FLS1000 fluorescence spectrophotometer (Edinburgh Instruments Ltd., U. K.) equipped with a continuous xenon lamp (450 W) as an excitation source and a liquid-nitrogen cooled NIR photomultiplier tube as the detector (Hamamatsu, R5509, InP/InGaAsP). The PL decay curve was also measured by FLS1000 instrument using a microsecond flash lamp (μF900) as the excitation source with data collection for 5000

counts. The quantum efficiency at room temperature was measured by an absolute PL quantum yield spectrometer (Quantaurus-QY Plus C13534-12, Hamamatsu Photonics).

X-ray Crystallography. Intensity data of five **Cu₄Pt₂** clusters were collected an Oxford Cryo stream system on a XtaLAB PRO MM007-DW diffractometer system equipped with HyPix-6000HE Hybrid Photon Counting (HPC) X-ray detector (Rigaku, Japan, Cu K α , graphite monochromator, $\lambda = 1.54 \text{ \AA}$). Absorption corrections were applied by using the program CrysAlis (multi-scan). The structures were solved by direct methods, and non-hydrogen atoms were refined anisotropically by least-squares on F^2 using the SHELXTL program.

III. Computational details

All calculations were performed by using density functional theory (DFT) and time-dependent density functional theory (TDDFT) within Gaussian09 suite of program². The hybrid functional B3LYP³ with dispersion correction⁴ (B3LYP-D3) and effective core potential and the corresponding basis set SDD⁵ was applied for Cu and Pt atoms, double zeta basis set 6-31G(d)⁶ was applied for other atoms. The geometries of **MeO-Cu₄Pt₂** in ground state were full optimized based on the X-ray crystal structures. The singlet vertical excitation energy and corresponding electron transitions as well as the frontier molecular orbital analysis was based on the ground state geometry. Based on the excitation energy, $E_{n \rightarrow m}$, and oscillator strength f, the absorption spectra were simulated using Gaussian functions. A full-width at half-maximum (FWHM), that is, the broadening of each peak (individual transition) of 0.30 eV was applied. The geometries of five deprotonated ligands were fully optimized as well. The corresponding electronic structure analysis were accomplished by Multiwfn 3.8⁷ and the visualization of the frontier molecular orbitals were done by Gaussview 6 and VMD 1.9.3⁸.

IV. Supporting figures

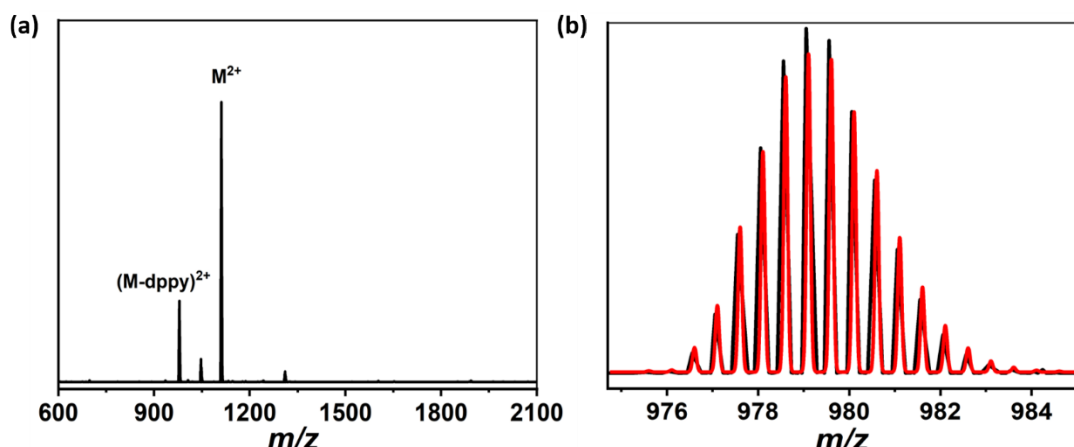


Figure S1. (a) ESI-MS spectra of **MeO-Cu₄Pt₂**. (b) Experimental (black trace) and simulated (red trace) isotopic patterns of $[\text{Cu}_4\text{Pt}_2(\text{MeO-C}_6\text{H}_5\text{-C}\equiv\text{C})_4(\text{dppy})_3]^{2+}$ (calcd. m/z 970.38), which is a fragment ion of **MeO-Cu₄Pt₂** after losing one dppy ligand.

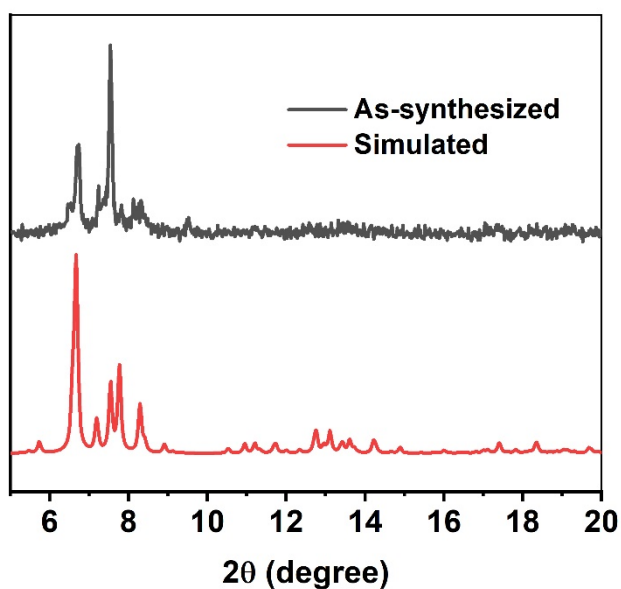


Figure S2. The comparison of simulated and as-synthesized PXRD patterns of **MeO-Cu₄Pt₂**.

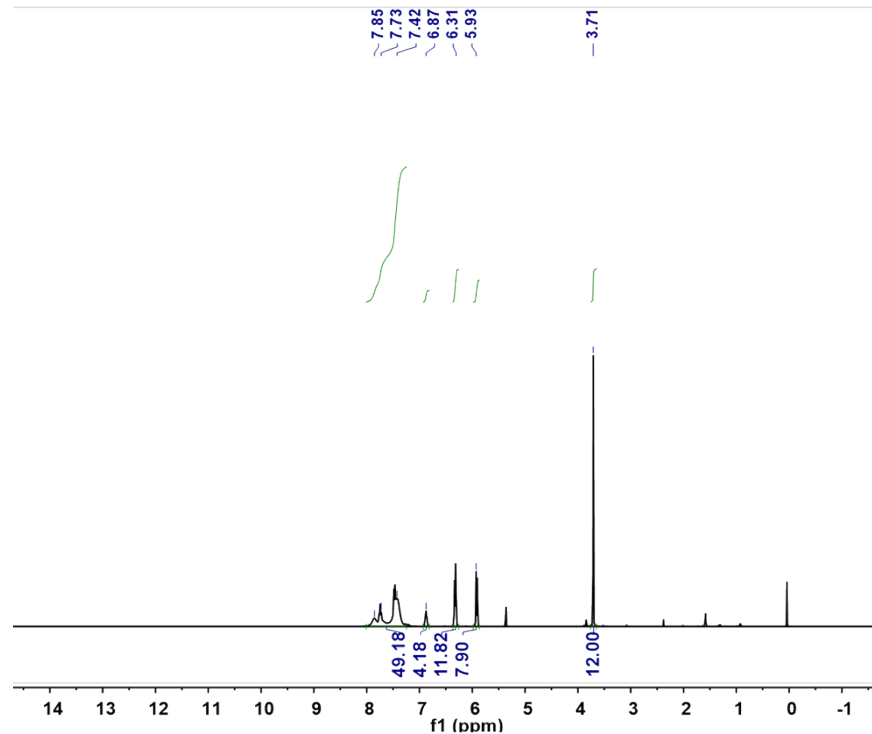


Figure S3. ¹H NMR spectrum of the MeO-Cu₄Pt₂.

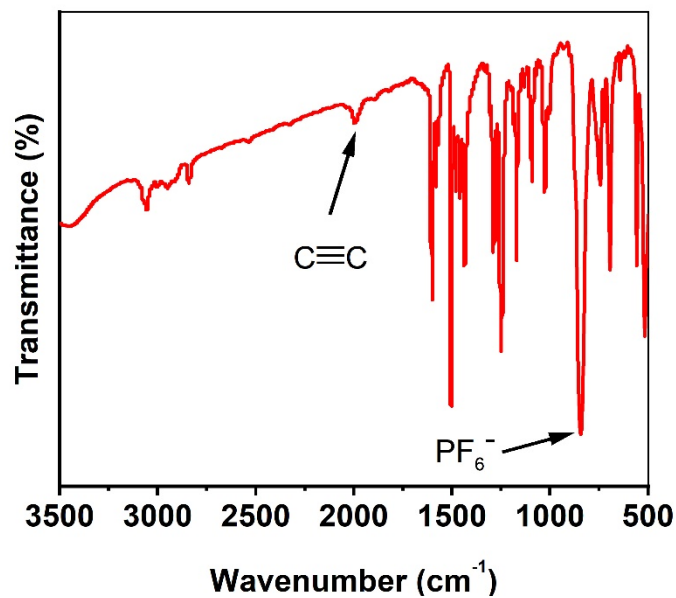


Figure S4 FT-IR spectra of MeO-Cu₄Pt₂.

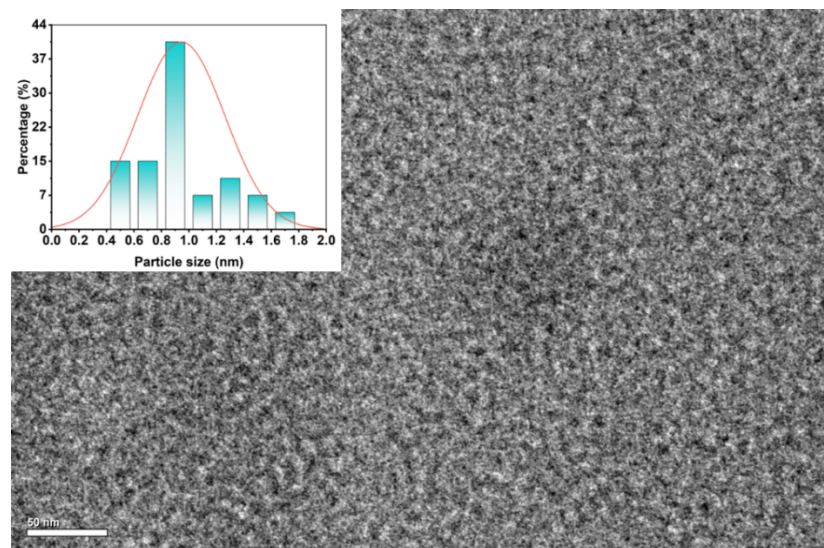


Figure S5. TEM image of $\text{MeO-Cu}_4\text{Pt}_2$ in acetone.

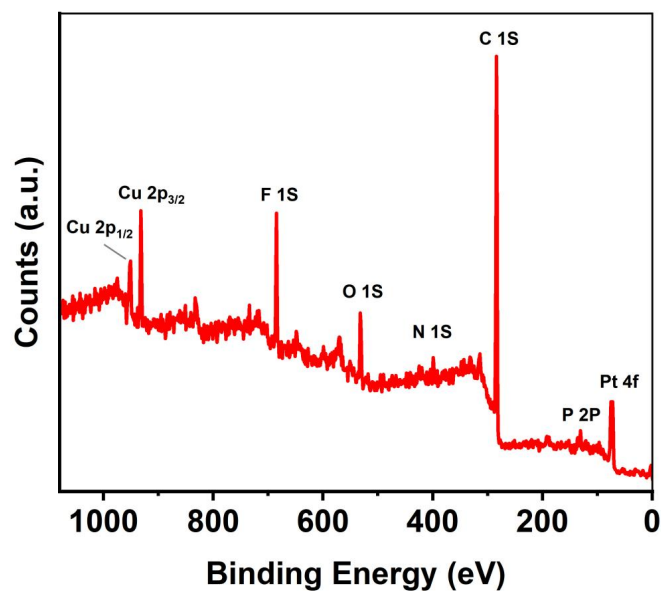


Figure S6. XPS full spectrum of $\text{MeO-Cu}_4\text{Pt}_2$.

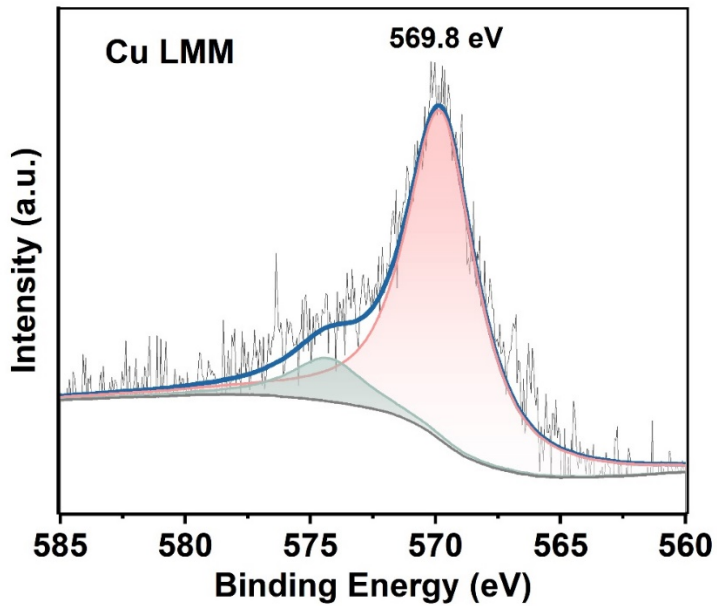


Figure S7. Cu LMM spectrum of **MeO-Cu₄Pt₂**.

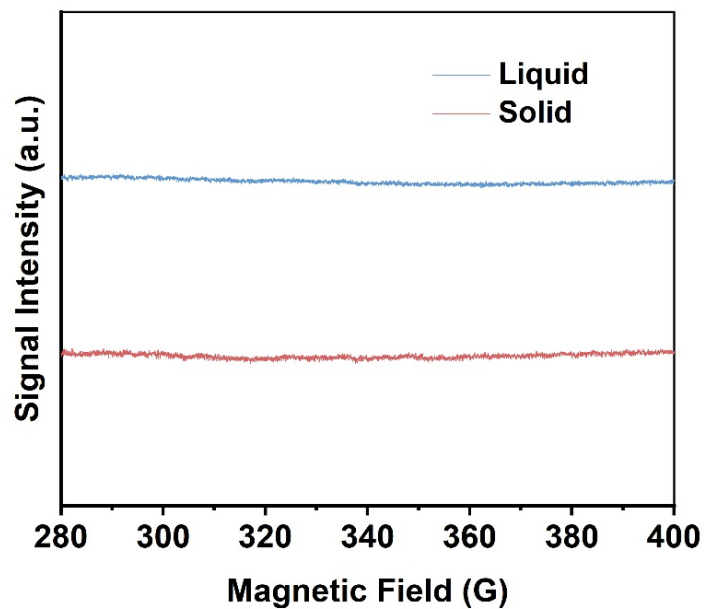


Figure S8. EPR spectra of **MeO-Cu₄Pt₂** in crystal state and in CH₂Cl₂ solution (2 mg/mL) under ambient conditions.

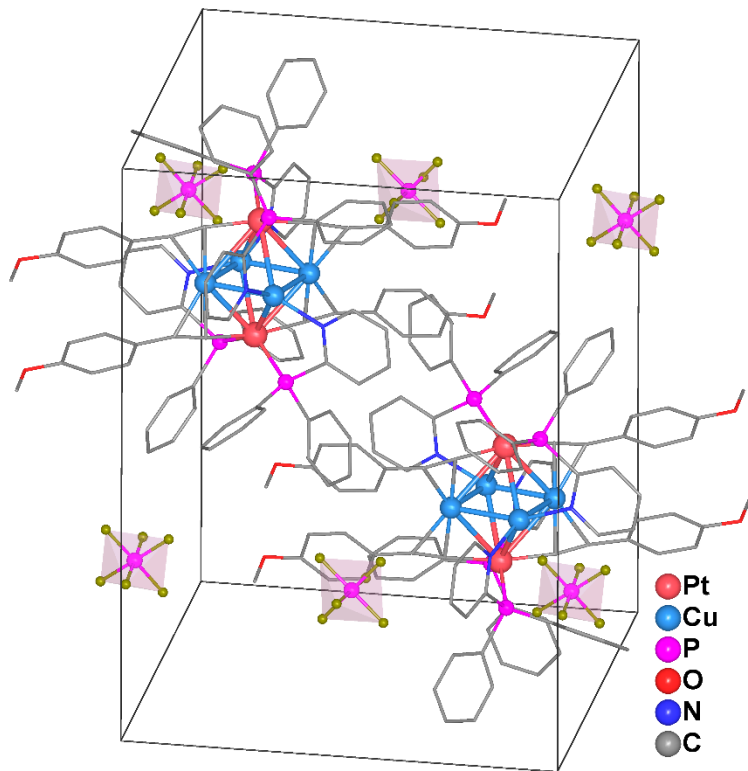


Figure S9. Two $[\text{Cu}_4\text{Pt}_2(\text{MeO}-\text{C}\equiv\text{C})_4(\text{dppy})_4]^{2+}$ cluster and four $[\text{PF}_6]^-$ anions exist in one unit cell. Color codes: Pt, pink; Cu, light blue; N, dark blue; P, purple; F, brown; O, red; C, gray.

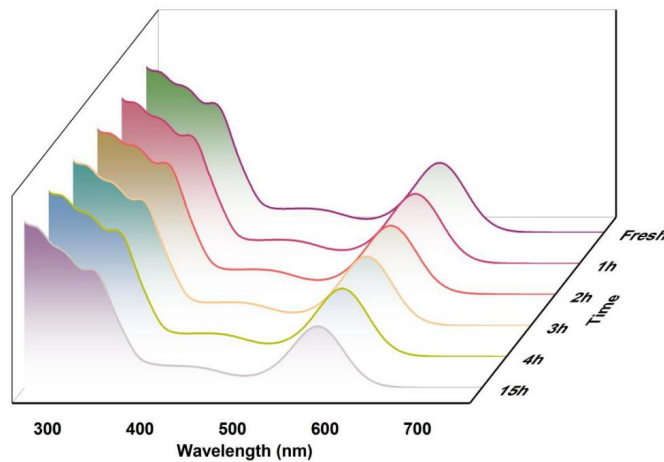


Figure S10. Monitoring solution-state stability of $\text{MeO-Cu}_4\text{Pt}_2$ cluster in CH_2Cl_2 under ambient conditions (25 °C in air).

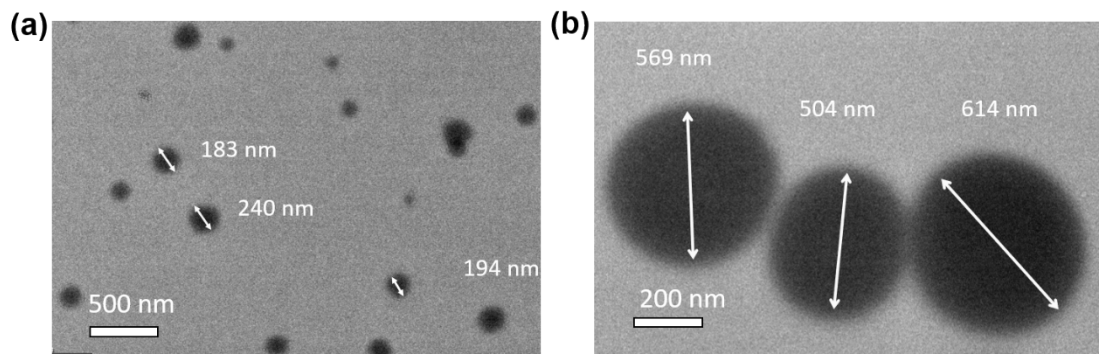


Figure S11. TEM images of **MeO-Cu₄Pt₂** in acetone with different proportions of Ethylene glycol (a) 45%; (b) 90%.

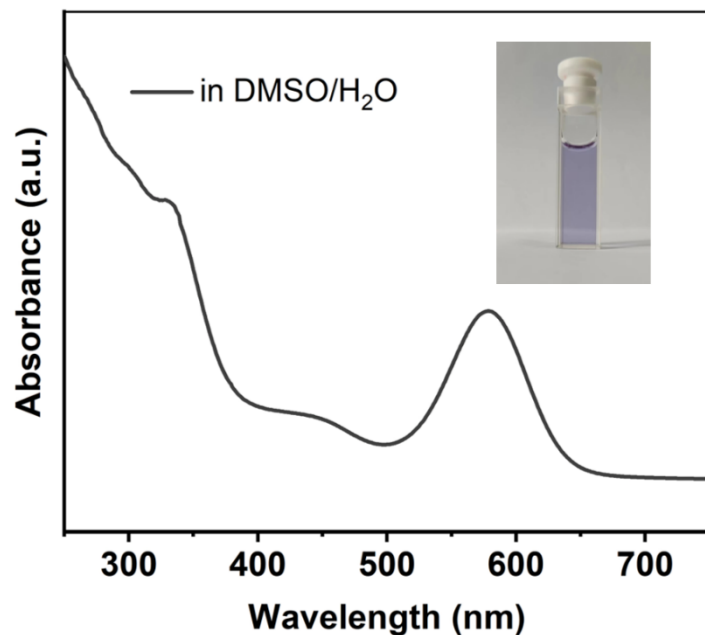


Figure S12. UV-vis absorption of **MeO-Cu₄Pt₂** in DMSO/H₂O (1:99, v/v).

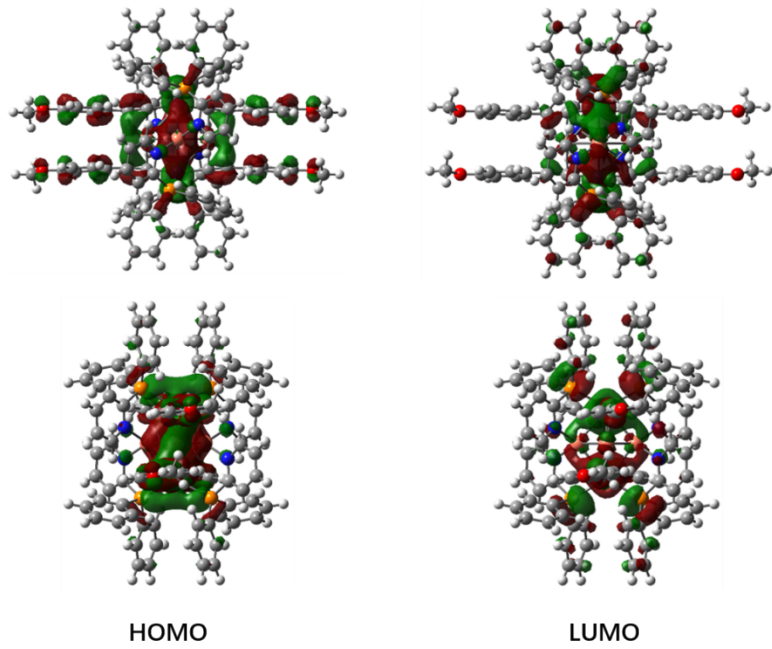


Figure S13. Two side views of frontier molecular orbitals for **MeO-Cu₄Pt₂**.

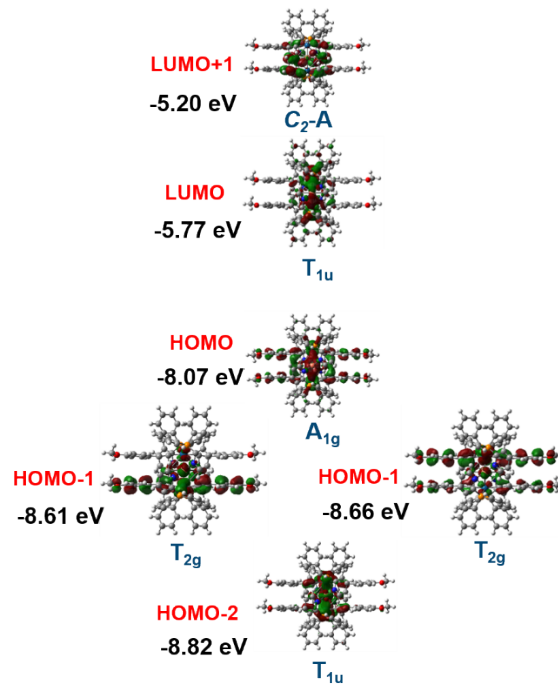


Figure S14. Partial frontier molecular orbital diagrams of **MeO-Cu₄Pt₂**.

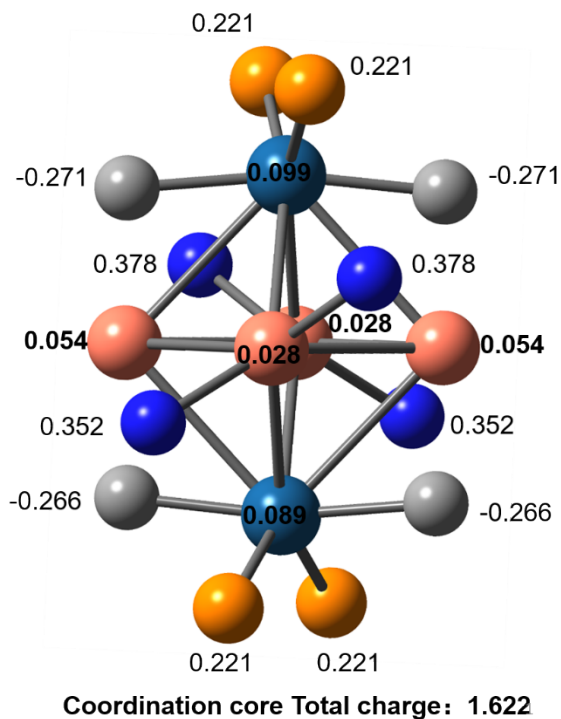


Figure S15. Bader charges of the metal atoms and the corresponding coordinated atoms in **MeO-Cu₄Pt₂**.

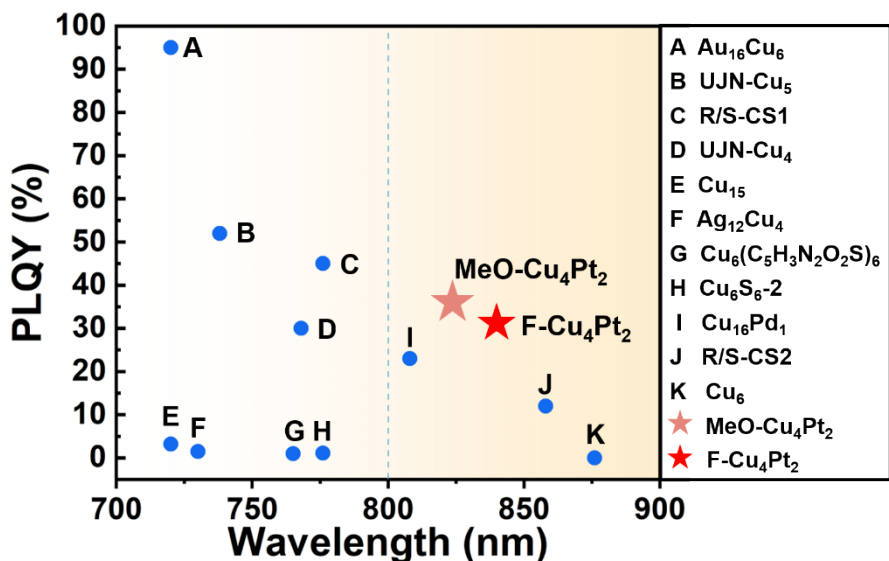


Figure S16. Summary of the PLQY for atomically copper-containing clusters with NIR emission.

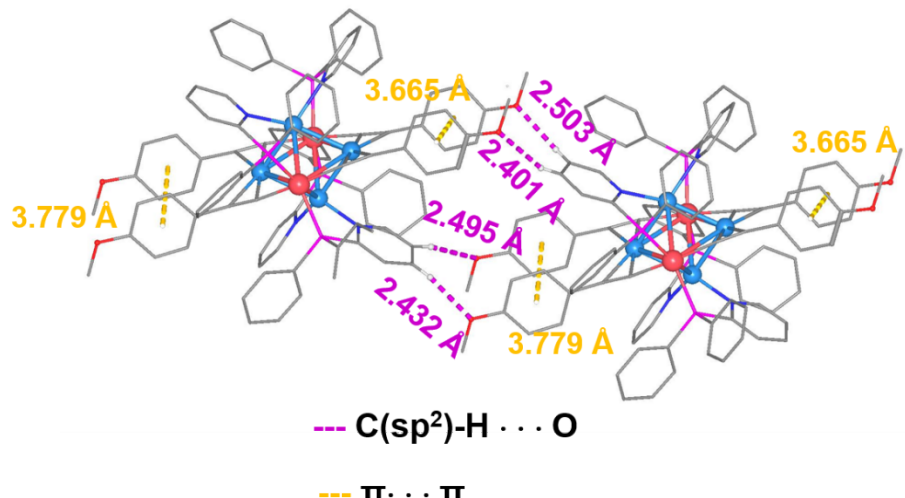


Figure S17. The intra- and intermolecular interactions in **MeO-Cu₄Pt₂**.

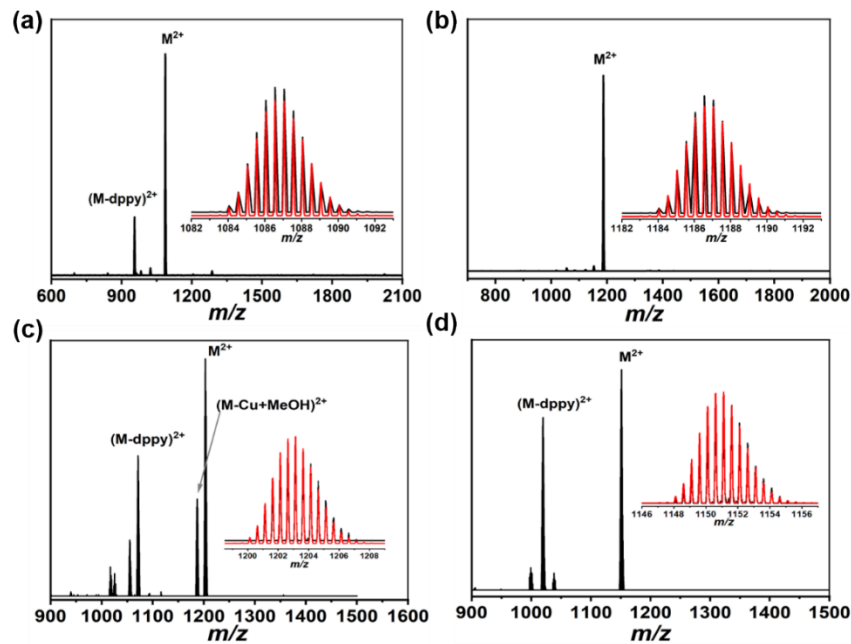


Figure S18. Positive mode ESI-MS spectra of **F-Cu₄Pt₂** (a), **CF₃-Cu₄Pt₂** (b), **BiPh-Cu₄Pt₂** (c), and **Nap-Cu₄Pt₂** (d). Insets: the measured (black line) and simulated (red line) isotopic distribution patterns of the corresponding molecular ion peaks.

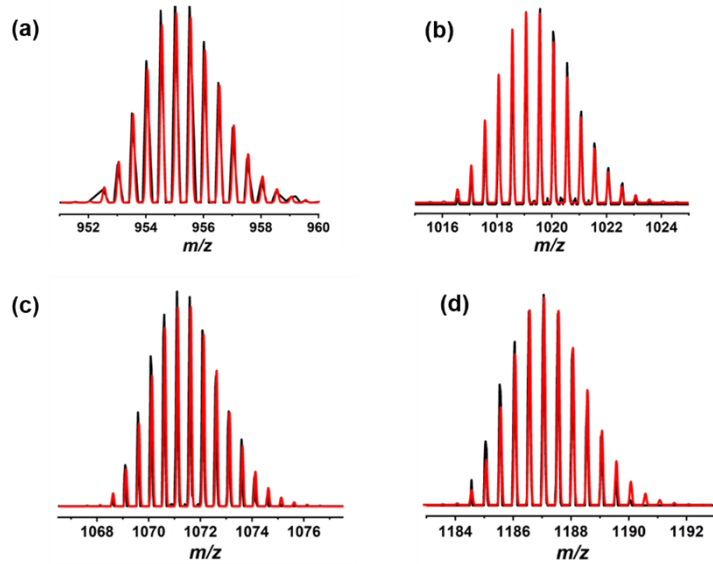


Figure S19. Experimental (black trace) and simulated (red trace) isotopic patterns of corresponding fragment ion peaks for (a) $[\text{Cu}_4\text{Pt}_2(\text{F-C}_6\text{H}_5\text{-C}\equiv\text{C})_4(\text{dppy})_3]^{2+}$ (calcd. m/z 955.31) of **F-Cu₄Pt₂**, (b) $[\text{Cu}_4\text{Pt}_2(\text{Nap-C}\equiv\text{C})_4(\text{dppy})_3]^{2+}$ (calcd. m/z 1019.45) of **Nap-Cu₄Pt₂**, (c) $[\text{Cu}_4\text{Pt}_2(\text{BiPh-C}\equiv\text{C})_4(\text{dppy})_3]^{2+}$ (calcd. m/z 1071.52) of **BiPh-Cu₄Pt₂**, and (d) $[\text{Cu}_3\text{Pt}_2(\text{BiPh-C}\equiv\text{C})_4(\text{dppy})_4\text{CH}_3\text{OH}]^{2+}$ (calcd. m/z 1187.41) of **Biph-Cu₄Pt₂**.

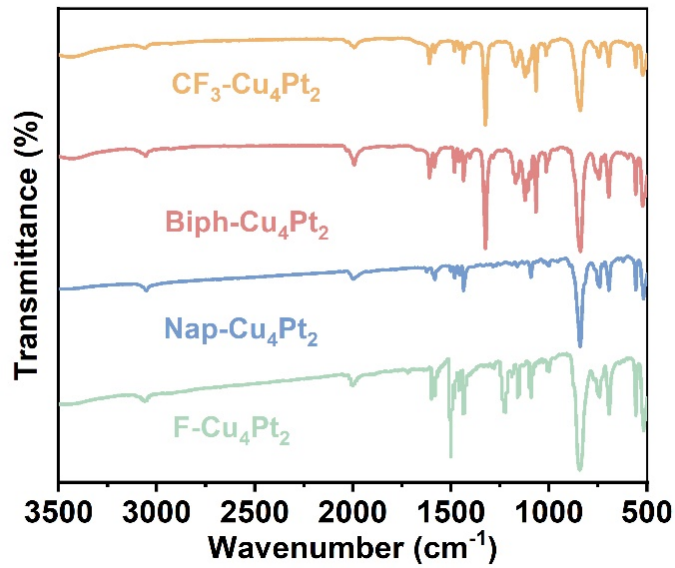


Figure S20 FT-IR spectra of four Cu_4Pt_2 crystal samples.

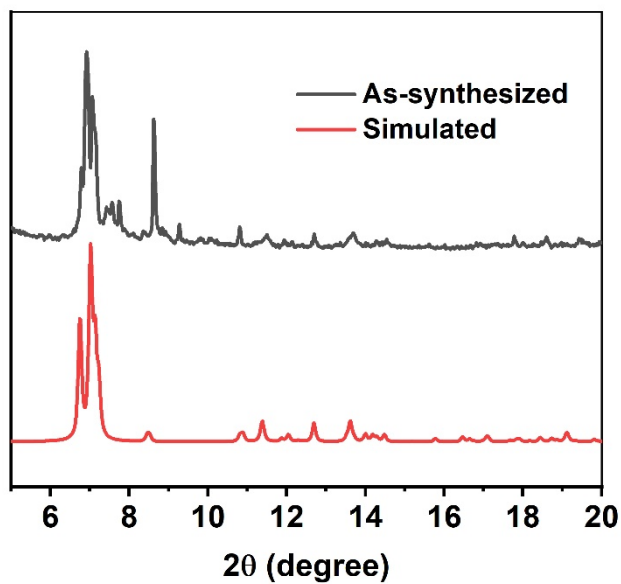


Figure S21. The comparison of simulated and as-synthesized PXRD patterns of $\text{F-Cu}_4\text{Pt}_2$.

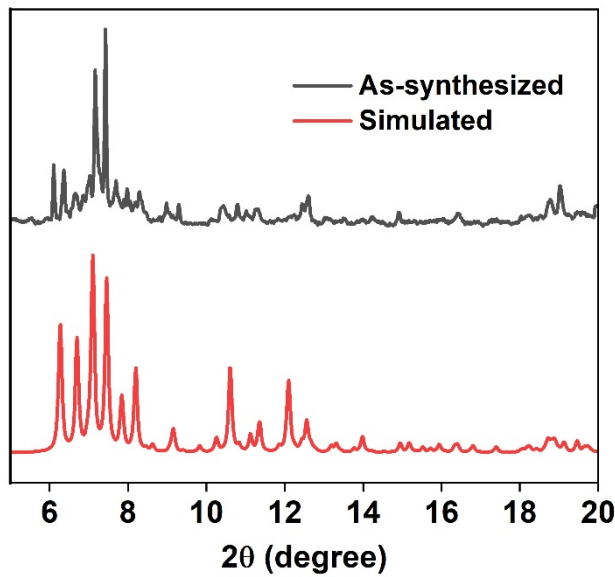


Figure S22. The comparison of simulated and as-synthesized PXRD patterns of $\text{CF}_3\text{-Cu}_4\text{Pt}_2$.

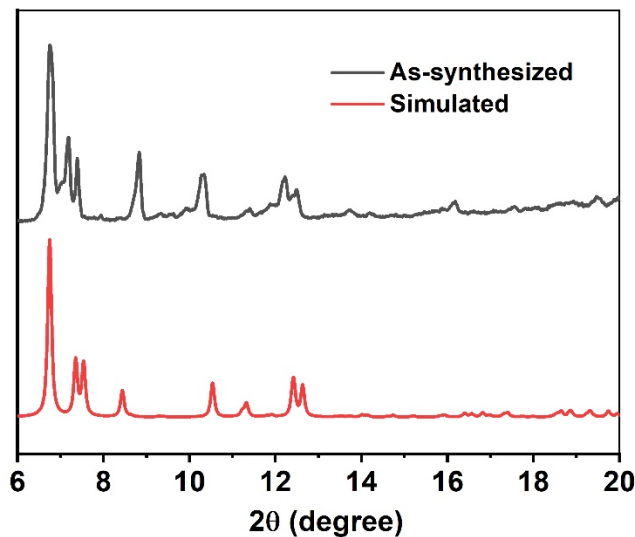


Figure S23. The comparison of simulated and as-synthesized PXRD patterns of $\text{Biph}\text{-Cu}_4\text{Pt}_2$.

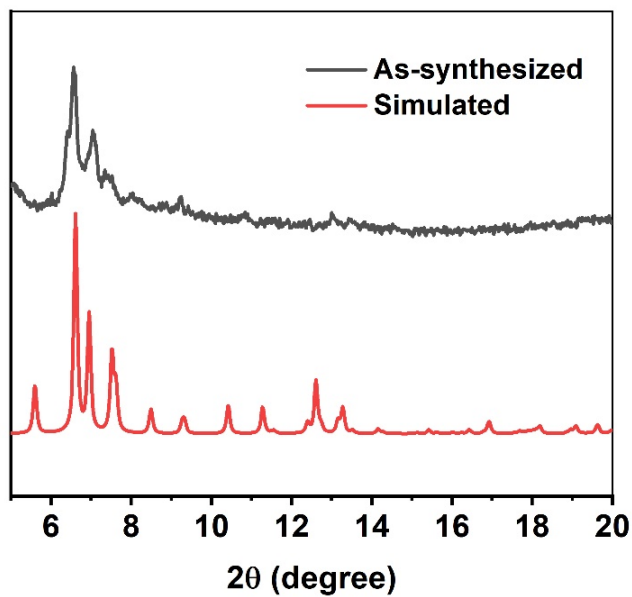


Figure S24. The powder XRD pattern of experimental (black) and simulation (red) of Nap-Cu₄Pt₂.

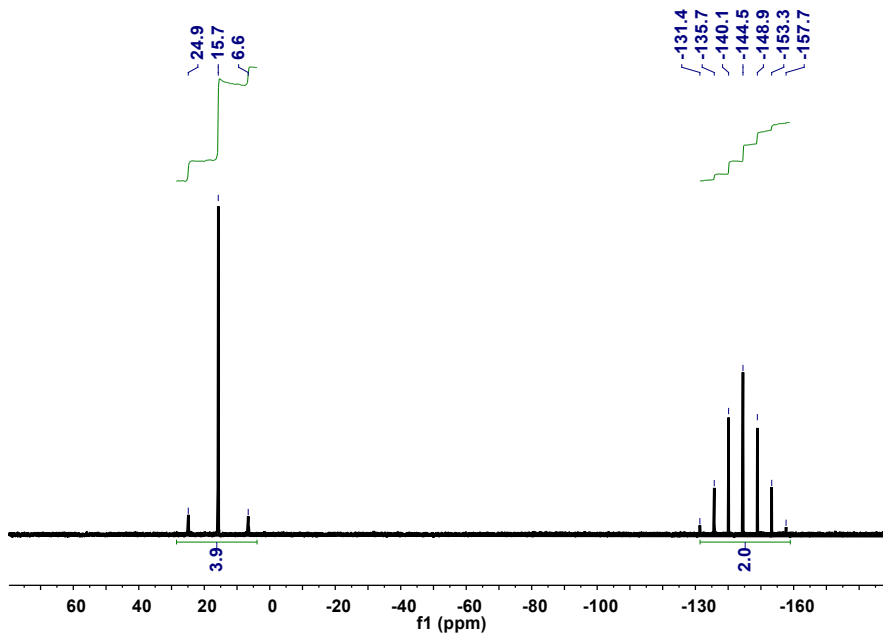


Figure S25. ³¹P NMR spectrum of the F-Cu₄Pt₂.

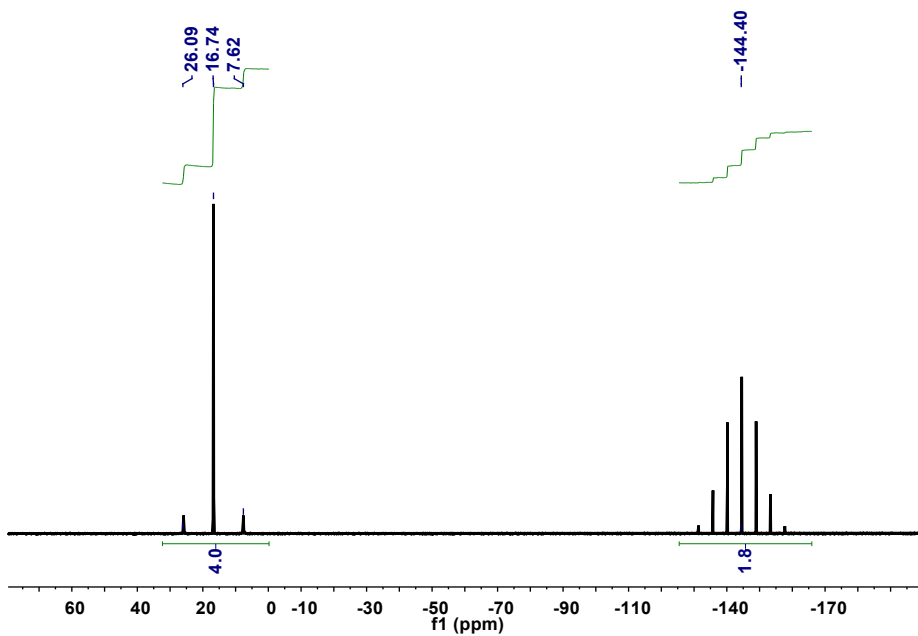


Figure S26. ^{31}P NMR spectrum of $\text{CF}_3\text{-Cu}_4\text{Pt}_2$.

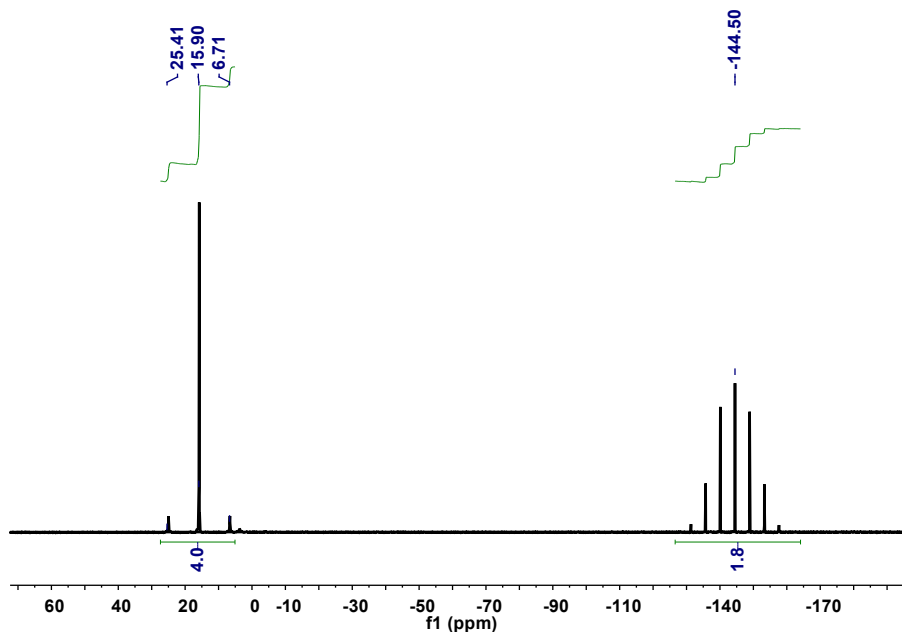


Figure S27. ^{31}P NMR spectrum of $\text{Nap-Cu}_4\text{Pt}_2$.

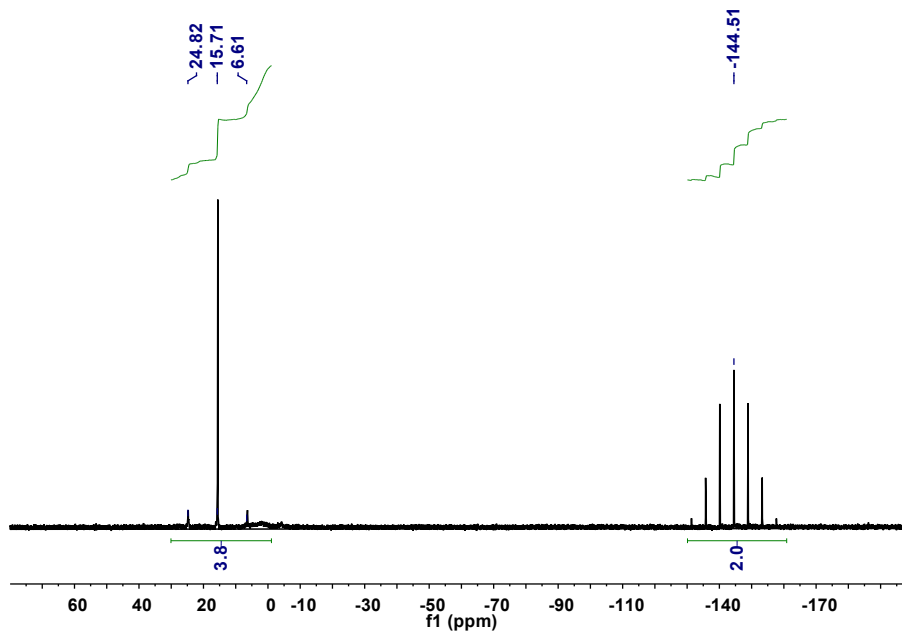


Figure S28. ^{31}P NMR spectrum of Biphenyl-Cu₄Pt₂.

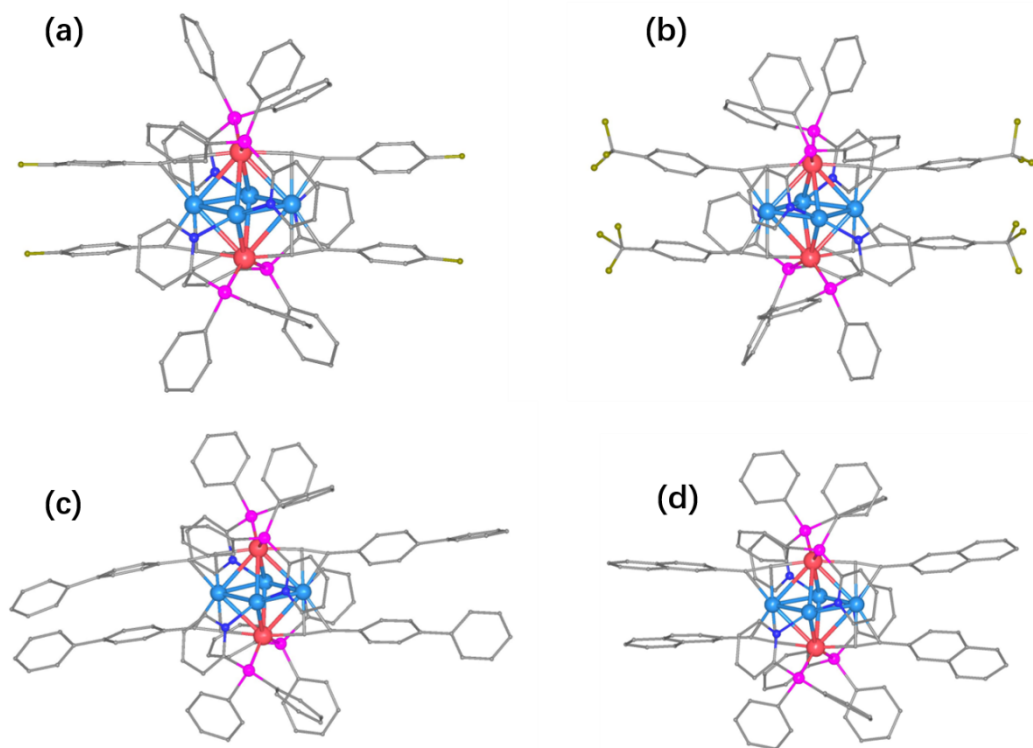


Figure S29. The total crystal structure of (a) F-Cu₄Pt₂, (b) CF₃-Cu₄Pt₂, (c) Nap-Cu₄Pt₂, and (d) Biphenyl-Cu₄Pt₂. Color codes: Pt, pink; Cu, light blue; N, dark blue; P, purple; F, green; O, red; C, gray.

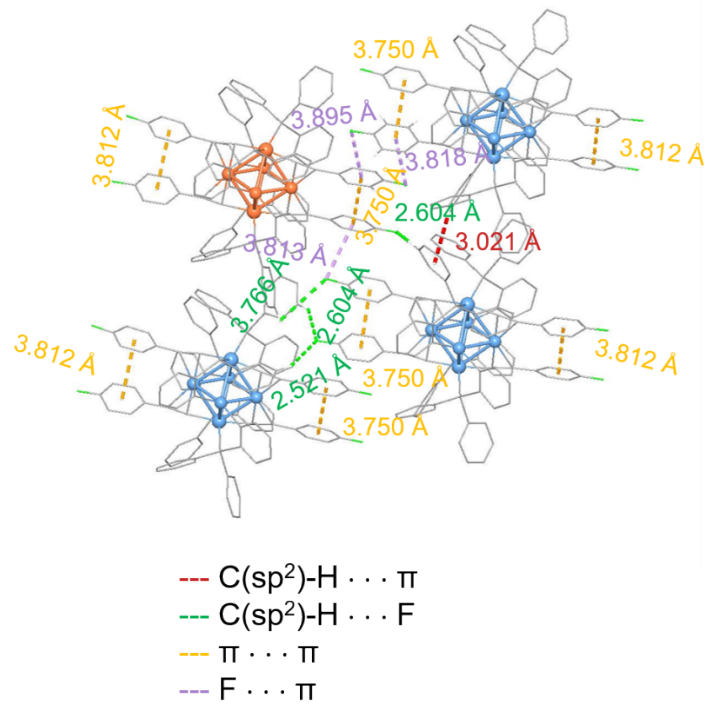


Figure S30. Illustration of the inter- and intramolecular interactions within $\text{F-Cu}_4\text{Pt}_2$.

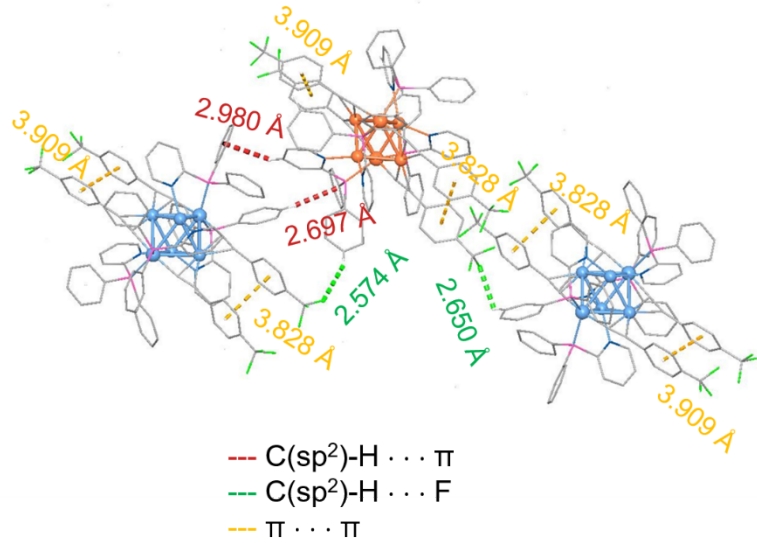


Figure S31. Illustration of the inter- and intramolecular interactions within $\text{CF}_3\text{-Cu}_4\text{Pt}_2$.

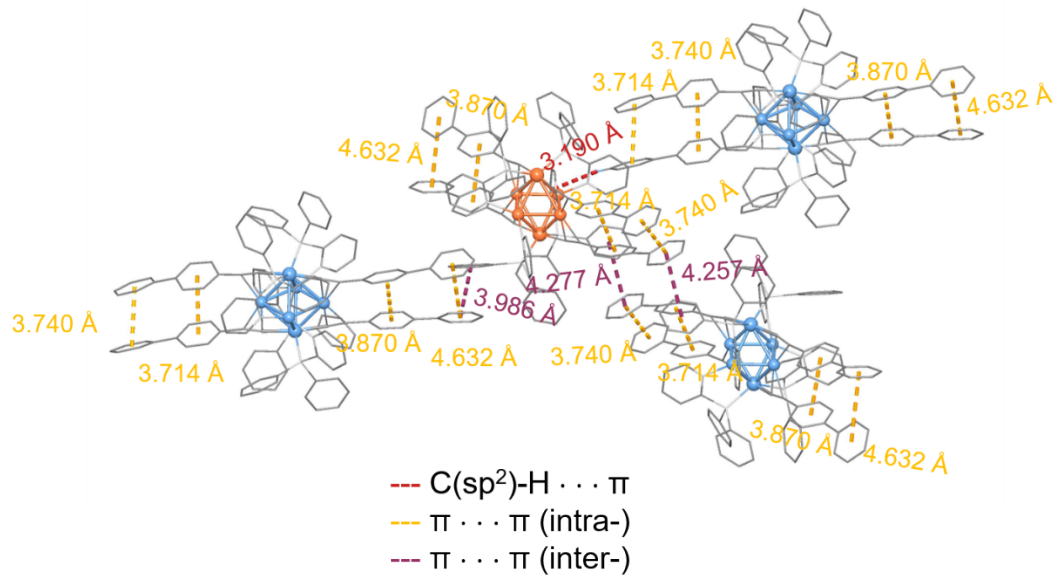


Figure S32. Illustration of the inter- and intramolecular interactions within **Biphenyl-Cu₄Pt₂**.

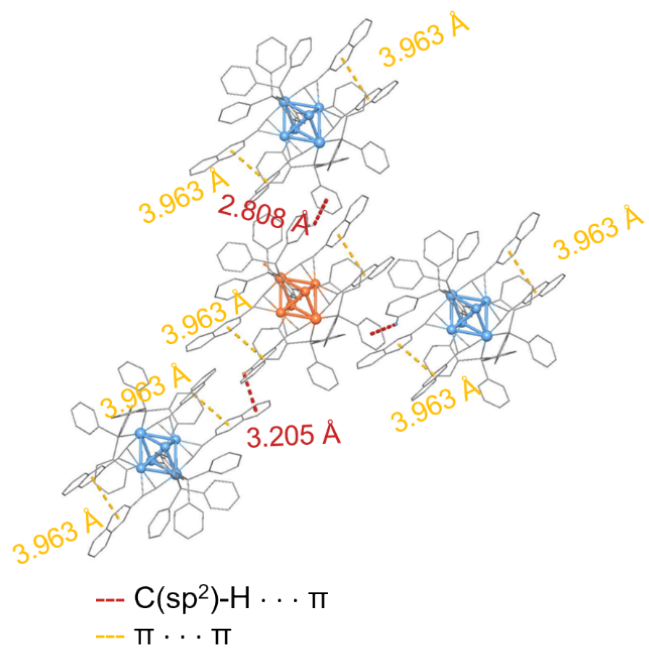


Figure S33. Illustration of the inter- and intramolecular interactions within **Naphthalene-Cu₄Pt₂**.

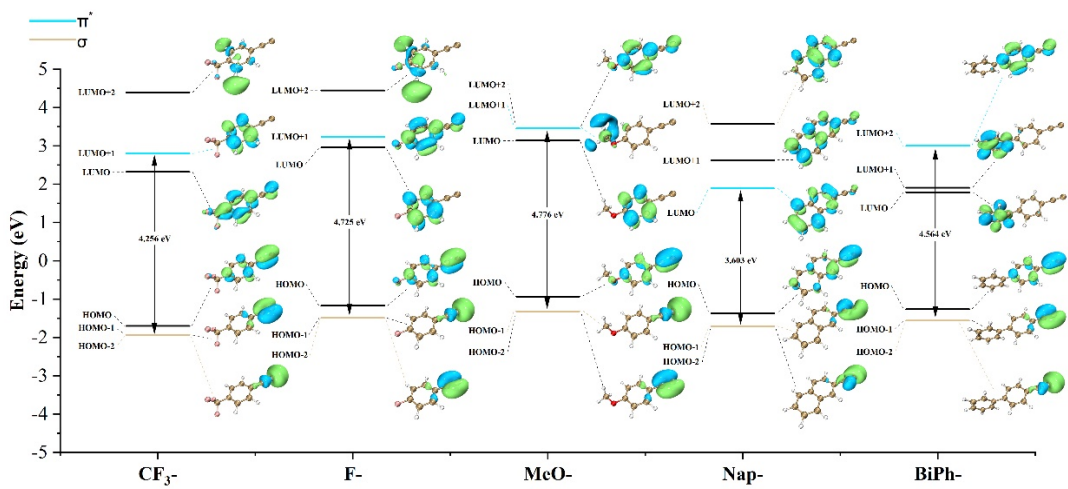


Figure S34. The molecular orbitals contour maps of the alkynyl ligands for $\text{F}/\text{CF}_3^-/\text{Biph}/\text{Nap}-\text{Cu}_4\text{Pt}_2$.

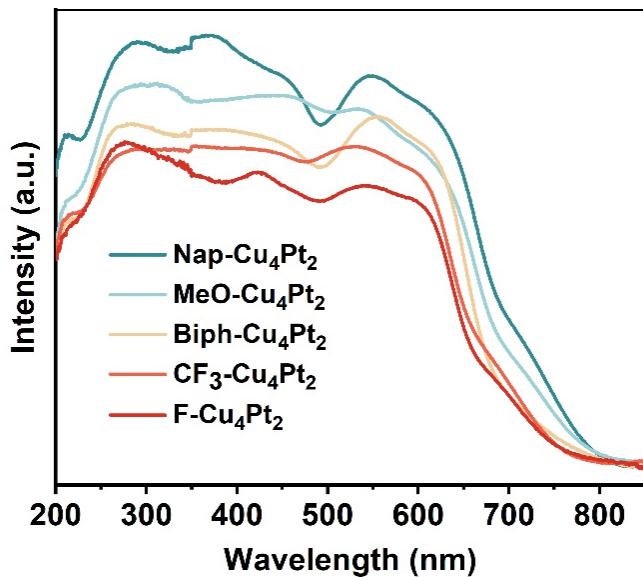


Figure S35. UV-vis DRS of five Cu_4Pt_2 crystal samples.

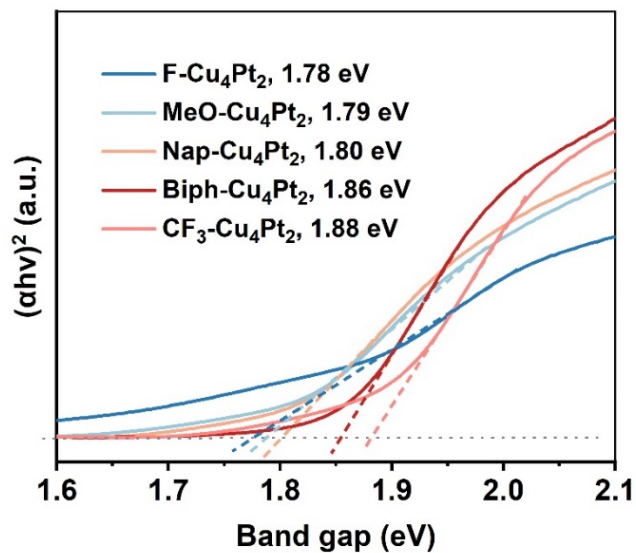


Figure S36. The optical gap of all R-Cu₄Pt₂ clusters.

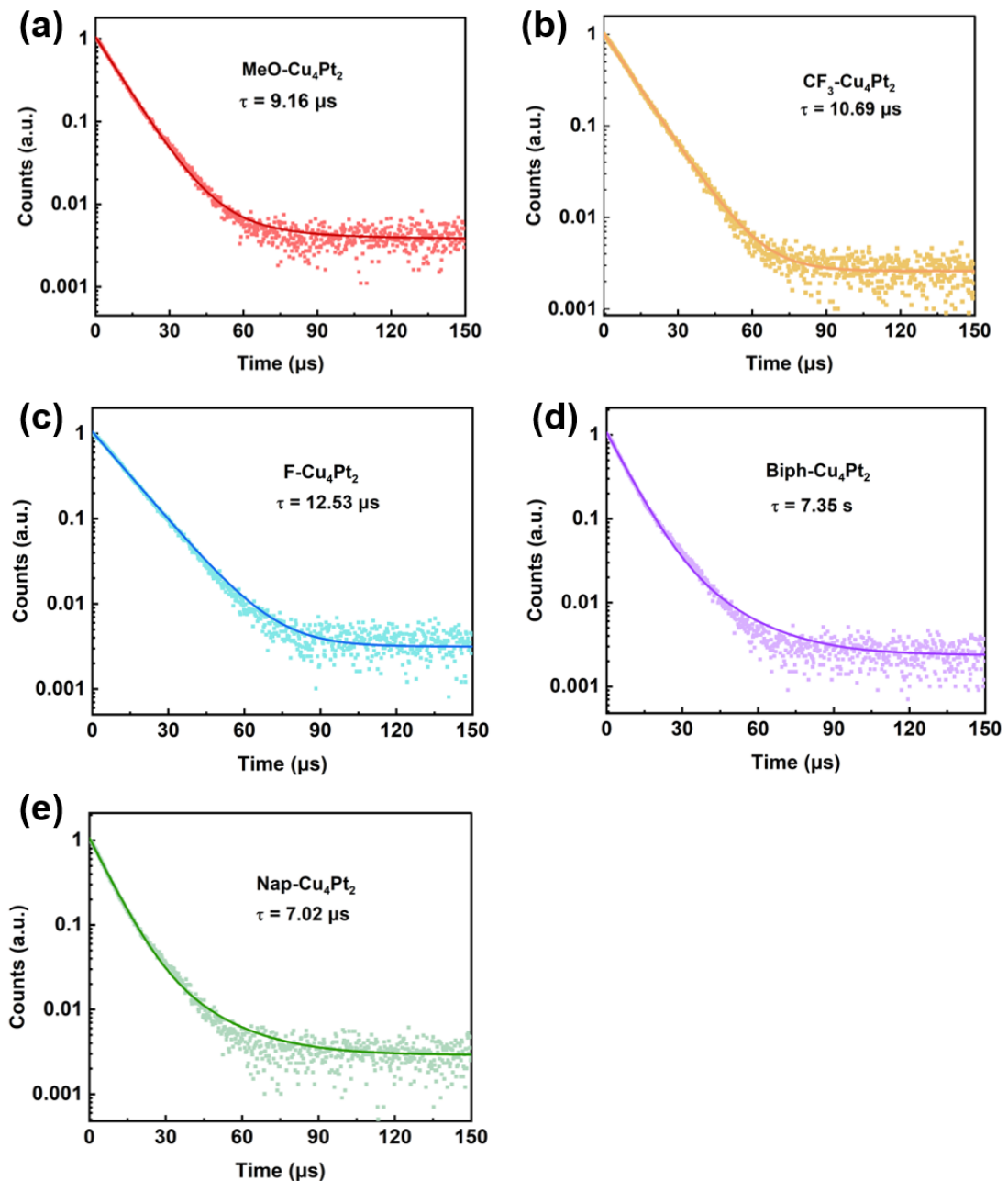


Figure S37. PL decay profiles of R- Cu_4Pt_2 in the crystalline state at room temperature, which uses the single exponential function.

Table S1. Summary of NIR luminescence properties of all reported atomically metal nanoclusters.

	Sample	State	λ_{em} (nm)	QY (%)	Ref.
A	Au ₁₆ Cu ₆	solution	720	95	9
B	UJN-Cu ₅	solid	738	52	10
C	R/S-CS1	solid	776	45	11
D	UJN-Cu ₄	solid	768	30	10
E	Cu ₁₅	solid	720	3.2	12
F	Ag ₁₂ Cu ₄	solid	730	1.5	13
G	Cu ₆ (C ₅ H ₃ N ₂ O ₂ S) ₆	solid	765	1	14
H	Cu ₆ S ₆ -2	solid	776	1.1	15
I	Cu ₁₆ Pd ₁	solid	823	23	16
J	R/S-CS2	solid	858	12	11
K	Cu ₆	solid	876	0.01	17
-	Cu ₂₈	solid	750	--	18
-	[(SbiPr ₃) ₄ Cu ₄ (I) ₄]	solid	711	--	19
-	Au ₁₃ Cu ₂	solid	1006	--	20
-	Au ₁₃ Cu ₄	solid	965	--	20
-	Cu _{15-a}	solid	726	--	21
-	Cu _{15-c}	solid	820	--	21
-	Cu ₃₁	solid	1250	--	22
-	Cu ₁₅	solid	710	--	23
	[Ag ₂₉ (BDT) ₁₂ (PPh ₃) ₄] ³⁻	solution	715	27.5	24
	[Au ₁₃ (NHCBn) ₉ Cl ₃] ²⁺	solution	730	16	25
	Pt ₁ Ag ₃₀ -SbF ₆	solution	740	54	26
	R /S-Ag ₁₇	solid	745	8	27
	[Au ₂₁ (SR) ₁₂ (PCP)] ^{+/PS}	solution	750	40	28
-	Ag ₂₉ (BDT) ₁₂ (TPP) ₄ NC	solution	770	39	29
	[Au ₂₀ (CZ-PrA) ₁₆] ²⁻	solution	820	1.42	30
	Au ₄₂ (SR) ₃₂	solution	875	3.2	31
	Au ₅₂ (<i>p</i> -MBT) ₃₂	solution	900-938	18.3	32
	Au ₃₈ S ₂ (S-Adm) ₂₀	solution	910	15	33
	Au ₂₄	solution	925	12	34
	[Au ₂₀ (CZ-PrA) ₁₆] ²⁻	solution	940	4.84	30
	Au ₂₅ rod	solution	990	8	35
	MeO-Cu ₄ Pt ₂	solid	824	36	this work
	F-Cu ₄ Pt ₂	solid	840	31	this work

Table S2. Crystal data and structure refinement for **MeO-Cu₄Pt₂**.

Identification code	MeO-Cu₄Pt₂
Empirical formula	C ₂₁₁ H ₁₇₄ N ₈ O ₈ F ₂₄ P ₁₂ Cl ₆ Cu ₈ Pt ₄
Formula weight	5278.59
Temperature/K	173.00(10)
Crystal system	triclinic
Space group	<i>P</i> -1
<i>a</i> /Å	14.8492(3)
<i>b</i> /Å	15.4702(4)
<i>c</i> /Å	22.7707(6)
$\alpha/^\circ$	89.501(2)
$\beta/^\circ$	84.631(2)
$\gamma/^\circ$	86.3650(19)
Volume/Å ³	5197.4(2)
<i>Z</i>	1
ρ_{calc} g/cm ³	1.686
μ /mm ⁻¹	8.008
<i>F</i> (000)	2602.0
Crystal size/mm ³	0.2 × 0.15 × 0.12
Radiation	CuK α (λ = 1.54184)
2 Θ range for data collection/°	6.836 to 130.288
Index ranges	-13 ≤ <i>h</i> ≤ 17, -14 ≤ <i>k</i> ≤ 18, -26 ≤ <i>l</i> ≤
Reflections collected	31741
Independent reflections	17173 [R_{int} = 0.0403, R_{sigma} = 0.0565]
Data/restraints/parameters	17173/36/1283
Goodness-of-fit on <i>F</i> ²	1.113
Final <i>R</i> indexes [$I \geq 2\sigma(I)$]	R_1 = 0.0393, wR_2 = 0.0976
Final <i>R</i> indexes [all data]	R_1 = 0.0520, wR_2 = 0.1030
Largest diff. peak/hole / e Å ⁻³	1.70/-0.94

Table S3. Crystal data and structure refinement for **F-Cu₄Pt₂**.

Identification code	F-Cu₄Pt₂
Empirical formula	C ₁₀₁ H ₇₄ N ₄ F ₁₆ P ₆ Cl ₂ Cu ₄ Pt ₂
Formula weight	2548.70
Temperature/K	173.00(10)
Crystal system	monoclinic
Space group	<i>P</i> 2 ₁ /c
<i>a</i> /Å	27.8806(11)
<i>b</i> /Å	14.6603(4)
<i>c</i> /Å	29.4612(11)
α /°	90
β /°	117.331(5)
γ /°	90
Volume/Å ³	10697.7(8)
<i>Z</i>	4
ρ_{calc} g/cm ³	1.582
μ /mm ⁻¹	7.562
<i>F</i> (000)	4992.0
Crystal size/mm ³	0.1 × 0.08 × 0.06
Radiation	CuKα (λ = 1.54184)
2Θ range for data collection/°	6.91 to 130.08
Index ranges	-32 ≤ <i>h</i> ≤ 23, -17 ≤ <i>k</i> ≤ 16, -34 ≤ <i>l</i> ≤ 33
Reflections collected	36737
Independent reflections	17554 [R_{int} = 0.0700, R_{sigma} = 0.0942]
Data/restraints/parameters	17554/384/1219
Goodness-of-fit on F ²	1.033
Final <i>R</i> indexes [I>=2σ (I)]	R_1 = 0.0947, <i>wR</i> ₂ = 0.2342
Final <i>R</i> indexes [all data]	R_1 = 0.1368, <i>wR</i> ₂ = 0.2639
Largest diff. peak/hole / e Å ⁻³	3.20/-2.32

Table S4. Crystal data and structure refinement for **CF₃-Cu₄Pt₂**.

Identification code	CF₃-Cu₄Pt₂
Empirical formula	C ₁₀₅ H ₇₄ N ₄ F ₂₄ P ₆ Cl ₂ Cu ₄ Pt ₂
Formula weight	2748.74
Temperature/K	173.00(10)
Crystal system	monoclinic
Space group	<i>P</i> 2 ₁ /c
<i>a</i> /Å	30.1604(8)
<i>b</i> /Å	14.9159(3)
<i>c</i> /Å	25.3705(8)
α /°	90
β /°	110.963(3)
γ /°	90
Volume/Å ³	10658.0(5)
<i>Z</i>	4
ρ_{calc} g/cm ³	1.713
μ /mm ⁻¹	7.753
<i>F</i> (000)	5376.0
Crystal size/mm ³	0.15 × 0.12 × 0.08
Radiation	Cu K α (λ = 1.54184)
2 Θ range for data collection/°	7.004 to 130.074
Index ranges	-35 ≤ <i>h</i> ≤ 23, -16 ≤ <i>k</i> ≤ 17, -29 ≤ <i>l</i> ≤ 28
Reflections collected	35641
Independent reflections	17574 [R_{int} = 0.0646, R_{sigma} = 0.0904]
Data/restraints/parameters	17574/244/1405
Goodness-of-fit on <i>F</i> ²	1.039
Final <i>R</i> indexes [<i>I</i> >=2 σ (<i>I</i>)]	<i>R</i> ₁ = 0.0596, <i>wR</i> ₂ = 0.1366
Final <i>R</i> indexes [all data]	<i>R</i> ₁ = 0.0948, <i>wR</i> ₂ = 0.1548
Largest diff. peak/hole / e Å ⁻³	1.46/-1.34

Table S5. Crystal data and structure refinement for **BiPh-Cu₄Pt₂**.

Identification code	BiPh-Cu₄Pt₂
Empirical formula	C ₁₃₈ H ₁₀₈ N ₄ F ₁₂ P ₆ Cu ₄ Pt ₂
Formula weight	2878.42
Temperature/K	100.00(11)
Crystal system	monoclinic
Space group	<i>P</i> 2 ₁ / <i>c</i>
<i>a</i> /Å	24.0292(3)
<i>b</i> /Å	23.4432(3)
<i>c</i> /Å	20.9407(3)
α /°	90
β /°	90.2540(10)
γ /°	90
Volume/Å ³	11796.2(3)
<i>Z</i>	4
ρ_{calc} g/cm ³	1.621
μ /mm ⁻¹	6.480
<i>F</i> (000)	5728.0
Crystal size/mm ³	0.15 × 0.1 × 0.1
Radiation	CuKα (λ = 1.54184)
2Θ range for data collection/°	5.266 to 119.988
Index ranges	-26 ≤ <i>h</i> ≤ 16, -26 ≤ <i>k</i> ≤ 26, -23 ≤ <i>l</i> ≤ 23
Reflections collected	49189
Independent reflections	16568 [R_{int} = 0.0542, R_{sigma} = 0.0682]
Data/restraints/parameters	16568/228/1473
Goodness-of-fit on F ²	1.021
Final <i>R</i> indexes [$I \geq 2\sigma(I)$]	R_1 = 0.0584, wR_2 = 0.1495
Final <i>R</i> indexes [all data]	R_1 = 0.0752, wR_2 = 0.1577
Largest diff. peak/hole / e Å ⁻³	2.08/-1.29

Table S6. Crystal data and structure refinement for **Nap-Cu₄Pt₂**.

Identification code	Nap-Cu₄Pt₂
Empirical formula	C ₁₁₆ H ₈₄ N ₄ F ₁₂ P ₆ Cu ₄ Pt ₂
Formula weight	2592.03
Temperature/K	100.01(11)
Crystal system	monoclinic
Space group	<i>C</i> 2/ <i>c</i>
<i>a</i> /Å	22.2403(3)
<i>b</i> /Å	19.9911(2)
<i>c</i> /Å	22.5255(3)
α /°	90
β /°	94.3900(10)
γ /°	90
Volume/Å ³	9985.6(2)
<i>Z</i>	4
ρ_{calc} g/cm ³	1.724
μ /mm ⁻¹	7.575
<i>F</i> (000)	5112.0
Crystal size/mm ³	0.15 × 0.1 × 0.08
Radiation	CuKα (λ = 1.54184)
2Θ range for data collection/°	5.952 to 156.528
Index ranges	-13 ≤ <i>h</i> ≤ 28, -24 ≤ <i>k</i> ≤ 21, -27 ≤ <i>l</i> ≤ 27
Reflections collected	22880
Independent reflections	10183 [R_{int} = 0.0353, R_{sigma} = 0.0390]
Data/restraints/parameters	10183/78/650
Goodness-of-fit on <i>F</i> ²	1.090
Final <i>R</i> indexes [$I \geq 2\sigma(I)$]	R_1 = 0.0469, wR_2 = 0.1313
Final <i>R</i> indexes [all data]	R_1 = 0.0527, wR_2 = 0.1350
Largest diff. peak/hole / e Å ⁻³	1.73/-1.60

Table S7. Optical parameters of the absorption transition of **Cu₄Pt₂** clusters in CH₂Cl₂.

Clusters	λ_{abs} (nm)	ϵ (M ⁻¹ cm ⁻¹) /10 ⁴
CF₃-Cu₄Pt₂	555	3.29
BiPh-Cu₄Pt₂	555	3.21
F-Cu₄Pt₂	559	2.72
Nap-Cu₄Pt₂	570	3.63
MeO-Cu₄Pt₂	572	3.15

References

- (1) Yuan, S.-F.; Luyang, H.-W.; Lei, Z.; Wan, X.-K.; Li, J.-J.; Wang, Q.-M. A Stable Well-Defined Copper Hydride Cluster Consolidated with Hemilabile Phosphines. *Chem. Commun.* **2021**, *57*, 4315–4318.
- (2) M. J. Frisch, G. W. Trucks H. B. Schlegel G. E. Scuseria M. A. Robb J. R. Cheeseman G. Scalmani V. Barone B. Mennucci G. A. Petersson H. Nakatsuji M. Caricato X. Li H. P. Hratchian A. F. Izmaylov J. Bloino G. Zheng J. L. Sonnenberg M. Hada M. Ehara K. Toyota R. Fukuda J. Hasegawa M. Ishida T. Nakajima Y. Honda O. Kitao H. Nakai T. Vreven J. A. Montgomery Jr J. E. Peralta F. Ogliaro M. Bearpark J. J. Heyd E. Brothers K. N. Kudin V. N. Staroverov R. Kobayashi J. Normand K. Raghavachari A. Rendell J. C. Burant S. S. Iyengar J. Tomasi M. Cossi N. Rega J. M. Millam M. Klene J. E. Knox J. B. Cross V. Bakken C. Adamo J. Jaramillo R. Gomperts R. E. Stratmann O. Yazyev A. J. Austin R. Cammi C. Pomelli J. W. Ochterski R. L. Martin K. Morokuma V. G. Zakrzewski G. A. Voth P. Salvador J. J. Dannenberg S. Dapprich A. D. Daniels Ö Farkas J. B. Foresman J. V. Ortiz J. Cioslowski; Fox, D. J. *Gaussian 09, Inc. Wallingford CT* **2009**.
- (3) Becke, Axel D.Density-functional thermochemistry. III. The role of exact exchange. *J. Chem. Phy.* **1993**, *98*, 5648-5652.
- (4) Grimme, Stefan; Antony, Jens; Ehrlich, Stephan; Krieg, Helge.A consistent and accurate ab initio parametrization of density functional dispersion correction (DFT-D) for the 94 elements H-Pu. *J. Chem. Phy.* **2010**, *132*, 154104.
- (5) Igel-Mann, G; Stoll, H; Preuss, H.Pseudopotentials for main group elements (IIa through VIIa). *Mol. Phys.* **1988**, *65*, 1321-1328.
- (6) Hariharan, Praveen C; Pople, John A.The influence of polarization functions on molecular orbital hydrogenation energies. *Theor. Chim. Acta* **1973**, *28*, 213-222.
- (7) Lu, Tian; Chen, Feiwu.Multiwfns: A multifunctional wavefunction analyzer. *J. Comput. Chem.* **2012**, *33*, 580-592.
- (8) Humphrey, William; Dalke, Andrew; Schulten, Klaus.VMD: Visual molecular dynamics. *J. Mol. Graph.* **1996**, *14*, 33-38.

- (9) Shi, W.-Q.; Zeng, L.; He, R.-L.; Han, X.-S.; Guan, Z.-J.; Zhou, M.; Wang, Q.-M. Near-Unity NIR Phosphorescent Quantum Yield from a Room-Temperature Solvated Metal Nanocluster. *Science* **2024**, *383*, 326–330.
- (10) Liu, G.-N.; Xu, R.-D.; Guo, J.-S.; Miao, J.-L.; Zhang, M.-J.; Li, C. Regulating the Near-Infrared Region to Visible-Light Emission by Adjusting Cuprophilic Interactions for Blue Light-Excited Phosphors. *J. Mater. Chem. C* **2021**, *9*, 8589–8595.
- (11) Han, Z.; Si, Y.; Dong, X.-Y.; Hu, J.-H.; Zhang, C.; Zhao, X.-H.; Yuan, J.-W.; Wang, Y.; Zang, S.-Q. Smart Reversible Transformations between Chiral Superstructures of Copper Clusters for Optical and Chiroptical Switching. *J. Am. Chem. Soc.* **2023**, *145*, 6166–6176.
- (12) Nematulloev, S.; Huang, R.; Yin, J.; Shkurenko, A.; Dong, C.; Ghosh, A.; Alamer, B.; Naphade, R.; Hedhili, M. N.; Maity, P.; Eddaoudi, M.; Mohammed, O. F.; Bakr, O. M. $[\text{Cu}_{15}(\text{PPh}_3)_6(\text{PET})_{13}]^{2+}$: A Copper Nanocluster with Crystallization Enhanced Photoluminescence. *Small* **2021**, *17*, 2006839.
- (13) Deng, G.; Lee, K.; Deng, H.; Bootharaju, M. S.; Zheng, N.; Hyeon, T. Alkynyl-Protected $\text{Ag}_{12}\text{Cu}_4$ Cluster with Aggregation-Induced Emission Enhancement. *J. Phys. Chem. C* **2022**, *126*, 20577–20583.
- (14) Hassanein, K.; Cappuccino, C.; Marchini, M.; Bandini, E.; Christian, M.; Morandi, V.; Monti, F.; Maini, L.; Ventura, B. Novel Cu(I)-5-Nitropyridine-2-Thiol Cluster with NIR Emission: Structural and Photophysical Characterization. *J. Phys. Chem. C* **2022**, *126*, 10190–10198.
- (15) Shan, X.-C.; Jiang, F.-L.; Yuan, D.-Q.; Wu, M.-Y.; Zhang, S.-Q.; Hong, M.-C. The Unusual Thermochromic NIR Luminescence of Cu(I) Clusters: Tuned by Cu–Cu Interactions and Packing Modes. *Dalton Trans.* **2012**, *41*, 9411.
- (16) Peng, S.; Yang, H.; Luo, D.; Ning, G.; Li, D. A Highly NIR Emissive $\text{Cu}_{16}\text{Pd}_1$ Nanocluster. *Small* **2023**, 2306863.
- (17) Ozawa, Y.; Mori, M.; Kiyooka, H.; Sugata, Y.; Ono, T.; Abe, M. Tetra- and Hexanuclear Copper(I) Iminothiolate Complexes: Synthesis, Structures, and Solid-State Thermochromic Dual Emission in Visible and near-Infrared Regions. *Chem. Pap.*

2020, *74*, 3717–3725.

- (18) Zhang, L. L.-M.; Zhou, G.; Zhou, G.; Lee, H.-K.; Zhao, N.; Prezhdo, O. V.; Mak, T. C. W. Core-Dependent Properties of Copper Nanoclusters: Valence-Pure Nanoclusters as NIR TADF Emitters and Mixed-Valence Ones as Semiconductors. *Chem. Sci.* **2019**, *10*, 10122–10128.
- (19) Taylor, W. V.; Cammack, C. X.; Shubert, S. A.; Rose, M. J. Thermoluminescent Antimony-Supported Copper-Iodo Cuboids: Approaching NIR Emission via High Crystallographic Symmetry. *Inorg. Chem.* **2019**, *58*, 16330–16345.
- (20) Anumula, R.; Reber, A. C.; An, P.; Cui, C.; Guo, M.; Wu, H.; Luo, Z.; Khanna, Shiv. N. Ligand Accommodation Causes the Anti-Centrosymmetric Structure of $\text{Au}_{13}\text{Cu}_4$ Clusters with near-Infrared Emission. *Nanoscale* **2020**, *12*, 14801–14807.
- (21) Fan, X.; Yuan, F.; Wang, J.; Cheng, Z.; Xiang, S.; Yang, H.; Zhang, Z. Structural Isomerization in Cu(I) Clusters: Tracing the Cu Thermal Migration Paths and Unveiling the Structure-Dependent Photoluminescence. *CCS Chem* **2023**, *5*, 350–360.
- (22) Jia, T.; Guan, Z.-J.; Zhang, C.; Zhu, X.-Z.; Chen, Y.-X.; Zhang, Q.; Yang, Y.; Sun, D. An Eight-Electron Superatomic Cu_{31} Nanocluster with Chiral Kernel and NIR-II Emission. *J. Am. Chem. Soc.* **2023**, *145*, 47–52.
- (23) Zhuo, H.; Su, H.; Cao, Z.; Liu, W.; Wang, S.; Feng, L.; Zhuang, G.; Lin, S.; Kurmoo, M.; Tung, C.; Sun, D.; Zheng, L. High-Nuclear Organometallic Copper(I)-Alkynide Clusters: Thermochromic Near-Infrared Luminescence and Solution Stability. *Chemistry A European J* **2016**, *22*, 17619–17626.
- (24) Khatun, E.; Ghosh, A.; Chakraborty, P.; Singh, P.; Boduzzaman, M.; Ganesan, P.; Natarajan, G.; Ghosh, J.; Pal, S. K.; Pradeep, T. A Thirty-Fold Photoluminescence Enhancement Induced by Secondary Ligands in Monolayer Protected Silver Clusters. *Nanoscale* **2018**, *10*, 20033–20042.
- (25) Narouz, M. R.; Takano, S.; Lummis, P. A.; Levchenko, T. I.; Nazemi, A.; Kaappa, S.; Malola, S.; Yousefalizadeh, G.; Calhoun, L. A.; Stamplecoskie, K. G.; Häkkinen, H.; Tsukuda, T.; Crudden, C. M. Robust, Highly Luminescent Au_{13} Superatoms Protected by N-Heterocyclic Carbenes. *J. Am. Chem. Soc.* **2019**, *141*, 14997–15002.

- (26) Zhang, M.-M.; Dong, X.-Y.; Wang, Z.-Y.; Luo, X.-M.; Huang, J.-H.; Zang, S.-Q.; Mak, T. C. W. Alkynyl-Stabilized Superatomic Silver Clusters Showing Circularly Polarized Luminescence. *J. Am. Chem. Soc.* **2021**, *143*, 6048–6053.
- (27) Wei, X.; Chu, K.; Adsetts, J. R.; Li, H.; Kang, X.; Ding, Z.; Zhu, M. Nanocluster Transformation Induced by SbF_6^- Anions toward Boosting Photochemical Activities. *J. Am. Chem. Soc.* **2022**, *144*, 20421–20433.
- (28) Li, Q.; Zhou, M.; So, W. Y.; Huang, J.; Li, M.; Kauffman, D. R.; Cotlet, M.; Higaki, T.; Peteanu, L. A.; Shao, Z.; Jin, R. A Mono-Cubooctahedral Series of Gold Nanoclusters: Photoluminescence Origin, Large Enhancement, Wide Tunability, and Structure–Property Correlation. *J. Am. Chem. Soc.* **2019**, *141*, 5314–5325.
- (29) Ishii, W.; Okayasu, Y.; Kobayashi, Y.; Tanaka, R.; Katao, S.; Nishikawa, Y.; Kawai, T.; Nakashima, T. Excited State Engineering in Ag_{29} Nanocluster through Peripheral Modification with Silver(I) Complexes for Bright Near-Infrared Photoluminescence. *J. Am. Chem. Soc.* **2023**, *145*, 11236–11244.
- (30) Zhou, S.; Gustavsson, L.; Beaune, G.; Chandra, S.; Niskanen, J.; Ruokolainen, J.; Timonen, J. V. I.; Ikkala, O.; Peng, B.; Ras, R. H. A. pH-Responsive Near-Infrared Emitting Gold Nanoclusters. *Angew. Chem. Int. Ed.* **2023**, *62*, e202312679.
- (31) Si, W.-D.; Zhang, C.; Zhou, M.; Tian, W.-D.; Wang, Z.; Hu, Q.; Song, K.-P.; Feng, L.; Huang, X.-Q.; Gao, Z.-Y.; Tung, C.-H.; Sun, D. Two Triplet Emitting States in One Emitter: Near-Infrared Dual-Phosphorescent Au_{20} Nanocluster. *Sci. Adv.* **2023**, *9*: eadg3587.
- (32) Luo, L.; Liu, Z.; Du, X.; Jin, R. Near-Infrared Dual Emission from the $\text{Au}_{42}(\text{SR})_{32}$ Nanocluster and Tailoring of Intersystem Crossing. *J. Am. Chem. Soc.* **2022**, *144*, 19243–19247.
- (33) Wan, X.; Xu, W. W.; Yuan, S.; Gao, Y.; Zeng, X.; Wang, Q. A Near-Infrared-Emissive Alkynyl-Protected Au_{24} Nanocluster. *Angew. Chem. Int. Ed.* **2015**, *54*, 9683–9686.
- (34) Li, Q.; Zeman, C. J.; Ma, Z.; Schatz, G. C.; Gu, X. W. Bright NIR-II Photoluminescence in Rod-Shaped Icosahedral Gold Nanoclusters. *Small* **2021**, *17*, 2007992.

(35) Wang, Y.; Liu, Z.; Mazumder, A.; Gianopoulos, C. G.; Kirschbaum, K.; Peteanu, L. A.; Jin, R. Tailoring Carbon Tails of Ligands on $\text{Au}_{52}(\text{SR})_{32}$ Nanoclusters Enhances the Near-Infrared Photoluminescence Quantum Yield from 3.8 to 18.3%. *J. Am. Chem. Soc.* **2023**, *145*, 26328–26338.